Silicon (2019) 11:2185–2192
https://doi.org/10.1007/s12633-018-0035-6

ORIGINAL PAPER

Deposition of Organosilicon-Plasma Coating onto Fine Graphite Micropowder with a Downstream Tubular PECVD Reactor

V. R. Giampietro[1] · M. Gulas[2] · V. Wood[3] · P. Rudolf von Rohr[1]

Received: 9 April 2018 / Accepted: 26 November 2018 / Published online: 1 February 2019
© Springer Nature B.V. 2019

Abstract

Fine graphite micropowder was processed in a downstream tubular reactor to perform a fast and homogeneous plasma-enhanced chemical vapor deposition of an organosilicon-plasma coating onto the powder surface. As a single process run results in the deposition of a non-continuous coating, consisting of a nanoparticle distribution, on the powder surface, the powder was repeatedly reprocessed until a continuous coating was obtained. The coating was imaged with focused ion-beam scanning electron microscopy and chemically characterized with Raman spectroscopy and X-ray photoelectron spectroscopy. The assessment of the powder flowability was also performed to investigate the roughness of the coated surface. The chemical characterization indicated that the coating is composed of amorphous hydrogenated silicon carbide with a little oxygen contamination.

Keywords PECVD · Micropowders · FIB-SEM · XPS

1 Introduction

Cold-plasma surface modifications are a versatile technique of material processing, which allows to functionalize and improve the surface properties of a multitude of materials with no alteration of their bulk properties [1–3]. Although cold-plasma technology succeeded in matching the request for industrial applications aiming to modify substrates with macroscopic (and often flat) surfaces, the processing of granular materials still poses grave drawbacks, mostly related to the difficult handling of the substrate material and the poor homogeneity of the obtained surface modification [4, 5]. In fact, powders (especially micropowders under 30 μm in diameter) often exhibit a poor flow behavior (flowability) and are therefore difficult to handle in a conventional plasma reactor for flat substrates, because of the particle aggregation and the large surface area to be exposed to the plasma [6, 7]. As one-half of the products and at least three-quarters of the raw materials in the chemical industry are in granular form, the solution of such drawbacks is the major challenge in the application of plasma processes to powder technology [8]. In fact, powder technology involves several types of materials in granular form (metals, metal oxides, pigments, polymers, minerals), which have important applications in various industrial fields (electronics, paints, cosmetics, biotechnology, recycling or blending of plastics, petrochemistry, pharmaceutics etc.); however, proper and homogeneous surface modifications are necessary in order to acquire the new surface properties required by the different applications, while the difficulty of the powder handling increases with decreasing particle sizes [6, 8, 9].

As regards glow-discharge-plasma processing, different types of reactors have been used to process powder substrates, such as mechanically-stirred reactors, rotary-drum reactors, fluidized-bed reactors, circulating-fluidized-bed reactors, downstream gravity reactors [7, 11–14]. Although the agitation of the batch of powder particles is a key factor to promote the plasma-particle contact and narrow the particle residence-time distribution in the reactor (and consequently improve the processing homogeneity), nevertheless both mechanically-stirred and rotary-drum reactors still show too broad a distribution, in addition to the formation of hot spots and the

✉ V. R. Giampietro
vitog@ipe.mavt.ethz.ch

[1] Institute of Process Engineering, ETH Zürich, Sonneggstrasse 3, 8092 Zurich, Switzerland

[2] Imerys Graphite & Carbon, Strada industriale 12, 6743 Bodio, Switzerland

[3] Department of Information Technology and Electrical Engineering, ETH Zürich, Gloriastrasse 35, 8092 Zurich, Switzerland

aggregation of finer particles [4, 5, 9, 13]. On the contrary, reactors based on fluidized beds are more suitable for favoring plasma-particle interactions, due to excellent interphase mass and heat transfer, narrower residence-time distribution and flat temperature profiles [9, 11, 13]. Circulating-fluidized-bed (CFB) reactors especially proved to be effective to optimize the plasma-enhanced chemical vapor deposition (PECVD) of coatings up to 1 μm in thickness onto particles with average diameter of the order of 100 μm [15, 16]. But for finer particles, the most suitable apparatus is hitherto the downstream reactor, which is superior to the other reactor types thanks to an extremely narrow residence-time distribution and a short average residence time of the particles [5]. In fact, a downstream plasma reactor basically consists of a vertical plasma tube, in which the powder to be processed continuously flows downwards concurrently with the gas feed and is uniformly distributed over the reactor cross section, with a short average residence time; such a typical pug-flow regime of the powder in the reactor dramatically favors the plasma-particle interactions and the process homogeneity, also enabling process throughput of several kilograms per hour [17, 18, 19]. On the contrary, CFB reactors show poor performance with powder particles below 30 μm in average diameter, as the powder fluidization is prevented by the increased interparticle cohesion; moreover, a large amount of the initial powder batch (also more than 50%) is lost due to the formation of a thick particle layer in stagnant zones of the reactor walls [20].

The technology of the downstream reactor was used by our group first to improve the wettability of polymeric powders (high-density polyethylene, copalyamide) by applying an oxygen plasma grafting; then to improve wettability, flowability and water-dissolution behavior of powders for the food and the pharmaceutical industry (lactose, salicylic acid) by performing PECVD of SiO_x-containing coatings [18, 19, 21]. As regards PECVD, the processing resulted in a distribution of nanoparticles of the order of 10 nm in size deposited on the surface of the powder particles, rather than a continuous layer, due to the short residence-time of the powder particles in the plasma zone [7, 22].

In the present study, we therefore aim to prove the feasibility of the downstream-reactor PECVD of a continuous organosilicon-plasma coating onto a fine micropowder of about 15 μm in average particle diameter, for which a CFB reactor is not suitable for the aforementioned reasons. The necessary increase in deposited mass was obtained by reprocessing the same powder batch 6 times with the downstream reactor, which was fed with and organosilicon monomer (hexamethyldisilane, abbrv. HMDS). The fine micropowder was graphite, of which we already succeeded in improving the flowability with single-run downstream-reactor PECVD processing [7]. Indeed, graphite is an important raw material for the industry, and recently silicon-bearing graphite has further raised the interest in this material, due to its promising mechanical, chemical and electrochemical properties [23, 24]. The powder surface was imaged with focused ion-beam scanning electron microscope (FIB-SEM). The surface chemical characterization was performed with Raman spectroscopy and X-ray photoelectron spectroscopy (XPS), two analytical techniques that are popularly used in the characterization of carbon materials and plasma coatings, respectively [25, 26]. In addition to these, the processed powder was characterized also by means of a flow-behavior (flowability) tester.

2 Experimental Section

The process scheme of the downstream tubular inductively-coupled RF plasma reactor utilized for the PECVD processing of graphite micropowder is shown in Fig. 1**,** with a photo of an Ar / HMDS plasma. A 1.5 m long glass tube, with an inner diameter of 40 mm (1), is the zone of ignition of glow-discharge plasma. The tube is cooled down with deionized water filling the gap between the plasma tube and the external tube (2). The discharge was driven by an inductively-coupled plasma (ICP) source, consisting of a radio-frequency (RF = 13.56 MHz) power generator (3), an impedance matching network (4) and a water-cooled copper coil (5). The reactor was evacuated to 3 Pa pressure with a two-stage (roots and a rotary vane pump) vacuum system (6), then the plasma feed gas was supplied and the system pressure was set to 150 Pa by means of a butterfly pressure-control valve (7). The feed gas (8) consisted of a 1:1 mixture of argon (PanGas, purity >99.999%) and HMDS (Sigma-Aldrich, purity >98%) set with flow controllers and mixer and kept constant at 500 sccm. The plasma discharge was ignited at 1200 W. Synthetic graphite micropowder (TIMREX® KS5–25, 15 μm average particle diameter) was then conveyed from the storage tank (9) into the plasma tube with a screw powder feeder (10) at a feed rate of 0.6 Kg/h, and mixed with the gas feed in a conical nozzle (11). In order to keep the powder residence time (and consequently the powder processing time) fixed at circa 0.1 s, both the total flow rate and the system pressure were kept constant [1, 7]. The processed powder was separated from the exhaust gas stream below the plasma zone by a downcomer (12), a cyclone (13) and a filter unit (14), and eventually collected in vessels (15). Once the storage tank was emptied, the reactor was stopped and repressurized, then the storage tank was refilled with the processed powder, in order to repeat the PECVD to augment the coating mass. Overall, 6 process repetitions (hereinafter referred to as runs) were performed on the same powder batch.

The imaging of the graphite particles was performed with a focused ion-beam scanning electron microscope (Zeiss NVision 40 FIB-SEM) equipped with a stub specimen holder, on which graphite was fixed by means of conductive stickers. A focused

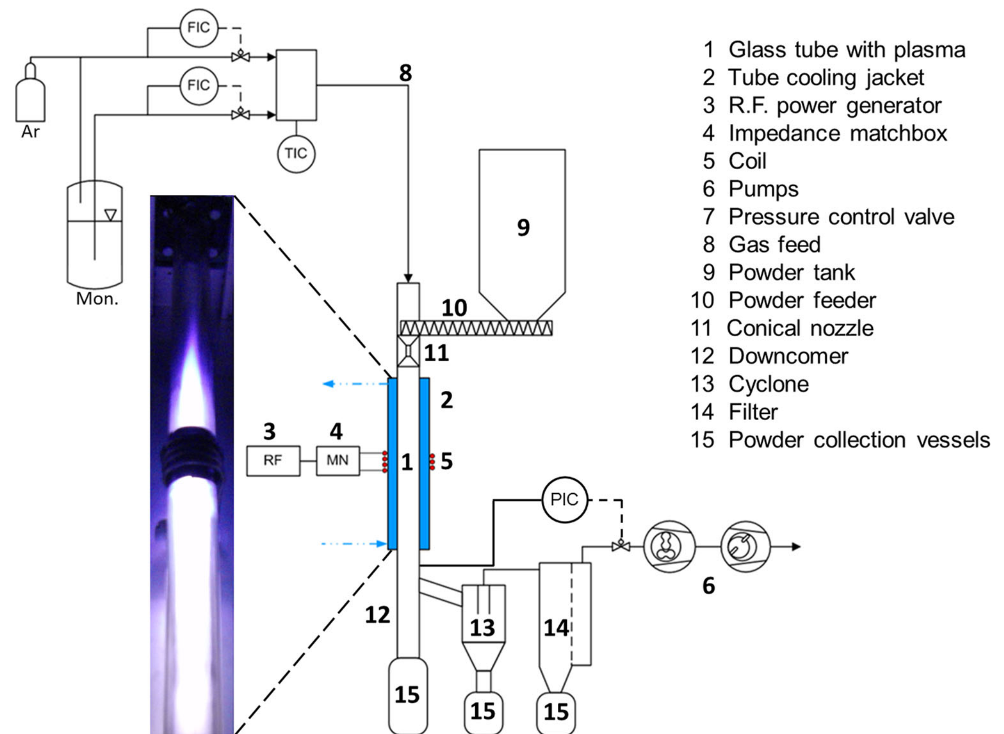

Fig. 1 Glow-discharge-plasma downstream reactor for fast processing of micropowders, adapted from [21]

beam of Ga^+ ions was operated at 30 KV and 80 pA in order to obtain milled cross-sections of the powder particles, which were subsequently imaged with SEM (tilt angle = 54°) at 5.0 kV electron-acceleration voltage, 60 μm aperture size, SE2 image mode, and 5.0 mm working distance.

Preliminary chemical and structural investigation of graphite surface was performed with a Raman spectrometer (inVia Raman microscope, Renishaw) equipped with an Ar-ion laser source. Graphite was placed on aluminum-tape-covered glass slide and focused with a 50x-objective microscope, then the spectra were acquired at an excitation laser wavelength of 514 nm (1800 l/mm grating), 2.5 mW power level and room temperature (10 s experiment time, 9 scans averaged).

Elemental composition and speciation of the graphite surface were determined by means of an X-ray photoelectron spectrometer (SIGMA Probe 2 XPS, Thermo Fisher) equipped with an ALPHA 110 hemispherical electron energy analyzer (110 mm mean radius). Graphite was placed and pressed with aluminum paper into bowl-shaped aluminum sample holders (6 mm diameter) without any sticker. The residual pressure in the spectrometer during the spectra acquisition was always below 10^{-7} Pa. A non-monochromatic Al Kα X-ray source (1486.6 eV) operating at 200 W was used for the spectra acquisition. Specimen emission angle and source-to-analyzer angles were respectively 0° and 50°, lens mode was large-area XPS, dwell time and energy step size were respectively 50 ms and 0.1 eV. The analyzer was operated in the fixed analyzer transmission mode, with pass energy set at 50 eV for the acquisition of the survey spectra (3 scans averaged) and at 20 eV for the acquisition of the high-resolution spectra (27 scans averaged). The spectrometer was calibrated and checked for linearity of the binding-energy scale according to the procedure reported in literature [27]. The full-width-at-half-maximum-height (FWHM) of the $Ag3d_{5/2}$ high-resolution signal acquired under the same experimental conditions as above was 1.3 eV.

The acquired XPS spectra were referenced to the adventitious carbon C1s signal at 285 eV (except those of the native graphite) and fitted by means of CasaXPS software with Gaussian–Lorentzian (GL) line shape, after application of Shirley background-subtraction routine. All fitting parameters were constrained except the peak intensity, and the binding energies of the signal components were assigned according to literature [28–33]. The quantitative analysis was performed for C1s, O1s and Si2p signal by considering the peak areas in the high-resolution spectra, which were corrected for Scofield photoionization cross sections, asymmetry function, attenuation length, and analyzer transmission function [33–37]. The relative sensitivity factors calculated for C1s signal, O1s signal and Si2p signal were respectively 1.00, 3.23 and 0.54. The maximum uncertainty of the measured binding energies equal to 0.2 eV [38]. The maximum errors of the sets of atomic percentages of a repeated quantitative analysis (3 repetitions) were chosen as uncertainties of the average values of the atomic percentages. The errors were subsequently propagated to calculate the uncertainties of the atomic-percentage ratios (C/O, Si/C and Si/O).

The flowability of graphite was assessed with a ring shear tester (RST-XS, Schulze Schüttguttechnik) equipped with a 30 ml shear cell, according to the procedure described by Schulze to quantify the powder flowability factor [39]. A pre-shear stress of 5000 Pa and consecutive shear stresses of 1000, 2500, and 4000 Pa were applied to the shear cell filled with the graphite specimen. Each measurement of flowability factor was repeated at least 3 times and the maximum error of the set of repetitions of each measurement was taken as an uncertainty of its average value.

3 Results and Discussion

The FIB-SEM images of the milled cross-sections of the particles of native and coated graphite are shown in Fig. 2. The first process run resulted in the deposition of a non-continuous coating, consisting in a nanoparticle distribution, on the substrate surface, which was already observed in previous studies about the downstream-reactor PECVD [7, 19]. The subsequent runs bring about a progressive coalescence growth of the plasma-deposited nanoparticles, until a rough continuous coating, on the order of 100 nm in thickness, is formed on the substrate surface (run 6). The roughness of the observed coating is supported by the flowability assessment of the processed graphite, reported in Table 1. In fact, the flowability factor of the native powder is 3.4 ± 0.1, typical value for cohesive non-flowing powders, and increases to 11.4 ± 0.3, typical value for free-flowing powders, already after the first run. [19]. Such a flowability improvement is a consequence of the nanoparticle distribution deposited on the powder surface, which can reduce the interparticle van der Waals attractive forces by roughening the particle surface [7]. But the progressive formation of a continuous coating (runs 2 to 6) does not invert the increasing trend of the flowability-factor, which reaches a plateau of 13.1 ± 0.1 (run 5). Therefore, the roughness of such a continuous coating is undiminished compared to that of the initial nanoparticle-coated surface (run 1), as it would have occurred if a smoother continuous coating had instead been formed [22].

The Raman spectra of native and processed graphite are shown in Fig. 3. The native graphite powder exhibits a spectrum having the following features: the weakest peak labelled D at about 1360 cm^{-1} (A_{1g} mode of the breathing vibration of the six-fold rings in disordered sp^2-carbon phases), a more intense and broader peak labelled 2D at ca. 2720 cm^{-1} (second harmonic of D) and the most intense and sharp peak labelled G at ca. 1580 cm^{-1} (E_{2g} mode of the in-plane bond-stretching vibration of sp^2-carbon atoms in monocrystalline graphite) [40–42]. Such features are preserved in the spectra of the graphite processed in the runs 1 to 3, but they gradually disappear in the subsequent spectra until a complete featureless spectrum is obtained (run 6). The gradual disappearance of the graphitic-carbon features in the

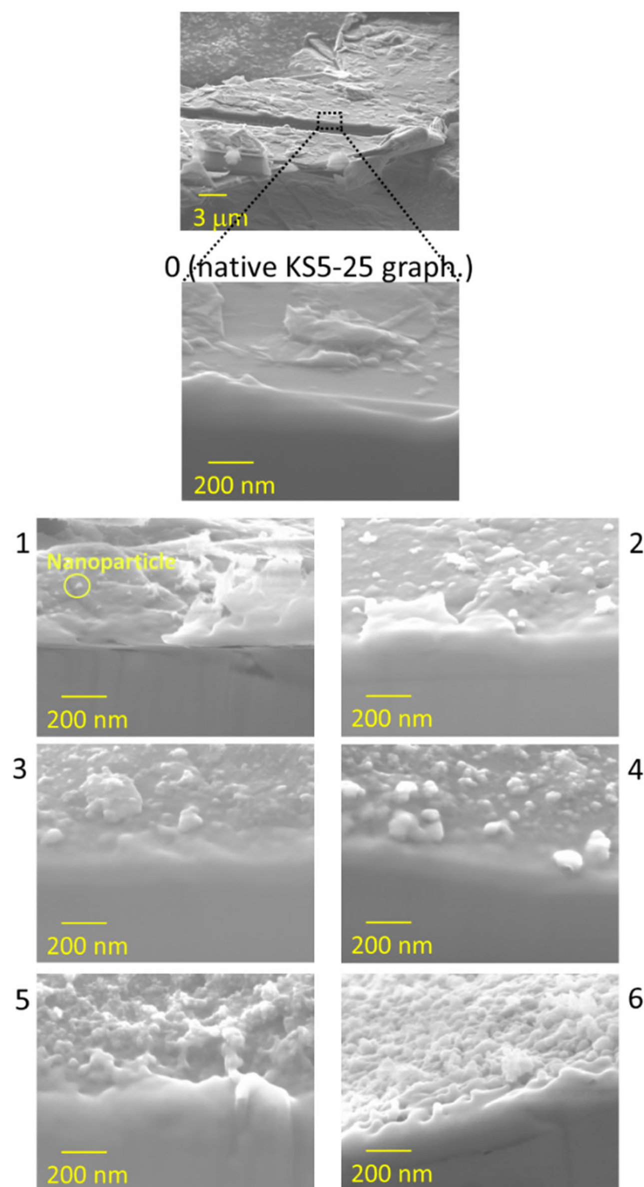

Fig. 2 FIB-SEM images of native and plasma-processed graphite micropowder labelled with the respective process-run numbers

Table 1 Values of the flowability factor of native and plasma-processed graphite micropowder

Process run	Flowability factor [−]
0 (native graphite)	3.4 ± 0.1
1	11.4 ± 0.3
2	11.6 ± 1.4
3	12.7 ± 0.3
4	12.8 ± 0.2
5	13.1 ± 0.1
6	13.1 ± 0.1

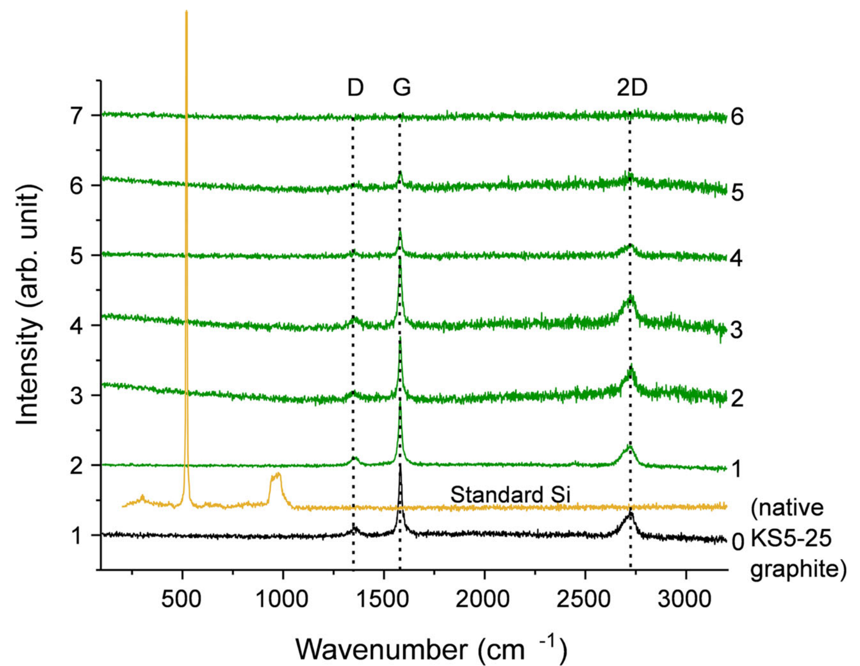

Fig. 3 Raman spectra of native and plasma-processed graphite micropowder labelled with the respective process-run numbers and highlighting the detected Raman signals

Raman spectra of Fig. 3 reveals an increasing structural disorder on the surface of the processed graphite, which clearly arises from the progressive formation of the coating observed in the FIB-SEM images of the graphite surface (Fig. 2) [41, 43]. When the graphitic-carbon features are completely lost (run 6), the graphite substrate is no longer Raman detectable, because the coating is now fully continuous and also thicker than the Raman sampling depth in it. The Raman analysis therefore supports the FIB-SEM inference that a continuous coating is formed on the graphite surface after 6 process runs. However, by comparing the Raman spectra of processed graphite to that of standard crystalline Si (Sigma-Aldrich, also shown in the figure), featuring a main sharp band at ca. 515 cm^{-1} between two smaller ones at ca. 300 and 970 cm^{-1}, no evident silicon signal is recognizable in these spectra, as well as no new carbon bands replacing the graphitic ones [40, 44]. Literature comparison thus suggests that such a coating might resemble amorphous hydrogenated silicon carbide (a-Si_xC_y:H, with $x \approx y$) [44–46]. In fact, the Raman spectra of such plasma-deposited coatings feature 3 typical bands (listed hereinafter according to their Raman efficiency), attributable to the C-C bonds (in the range 1300–1600 cm^{-1}), the Si-Si bonds (300–600 cm^{-1}) and the Si-C bonds (600–100 cm^{-1}), respectively [44, 45]. Si-Si and C-C bands can be clearly detected respectively in silicon-rich and carbon-rich samples, while the Si-C band is more difficult to detect [44, 45]. Since in nearly-stoichiometric coatings the Si-C bonds are predominant, the Raman spectrum of such coatings can therefore only feature a noisy signal in the range corresponding to the Si-C band [45, 46]. Moreover, a continuous amorphous silicon-carbide coating has a Raman sampling depth of about 50 nm (at the used excitation laser wavelength of 514 nm), i.e. significantly lesser than the present FIB-SEM-estimated thickness (~100 nm), which is in accord with the aforementioned consideration about the observed disappearance of the graphite features in its Raman spectrum [47, 48].

Since the coating detected on graphite processed in run 6 is continuous and ~100 nm thick, it can be considered a surface-uniform sample whose elemental concentrations are essentially homogenous within the XPS sampling depth, which is <10 nm for all XPS-investigated elements in the present work, and the lateral resolution (> 100 nm) [38]. Therefore, the XPS quantitative analysis of the element signals can be performed in this case without ambiguity, since any interference of the graphitic substrate can in principle be ruled out. The XPS analysis of the obtained continuous coating (run-6 graphite) supports the aforesaid conclusion drawn from the Raman analysis. The survey spectrum (not shown) of the native graphite features a photoelectron-emission signal from carbon at a binding energy (BE) of 284 eV (C1s), whereas the survey spectrum of the run-6 graphite features signals from silicon and oxygen too, at 102 eV (Si2p, beside Si1s at around 150 eV) and 532 eV (O1s), respectively [28]. The same set of elemental signals was found also in the spectra of the graphite processed in the runs 1 to 5. Hydrogen is not mentioned as it is not XPS detectable, whereas the oxygen contamination is a common feature of plasma coatings, arising from the oxygen embedding into the plasma-deposited material which occurs during either the deposition process or the subsequent coating air exposure [1, 38, 46]. The atomic-percentage ratios of the coating, calculated from the high-resolution spectra of the run-6 graphite (Fig. 4), are reported in Table 2. The Si/C atomic-percentage ratio is ca. 0.8, in accord with the interpretation of

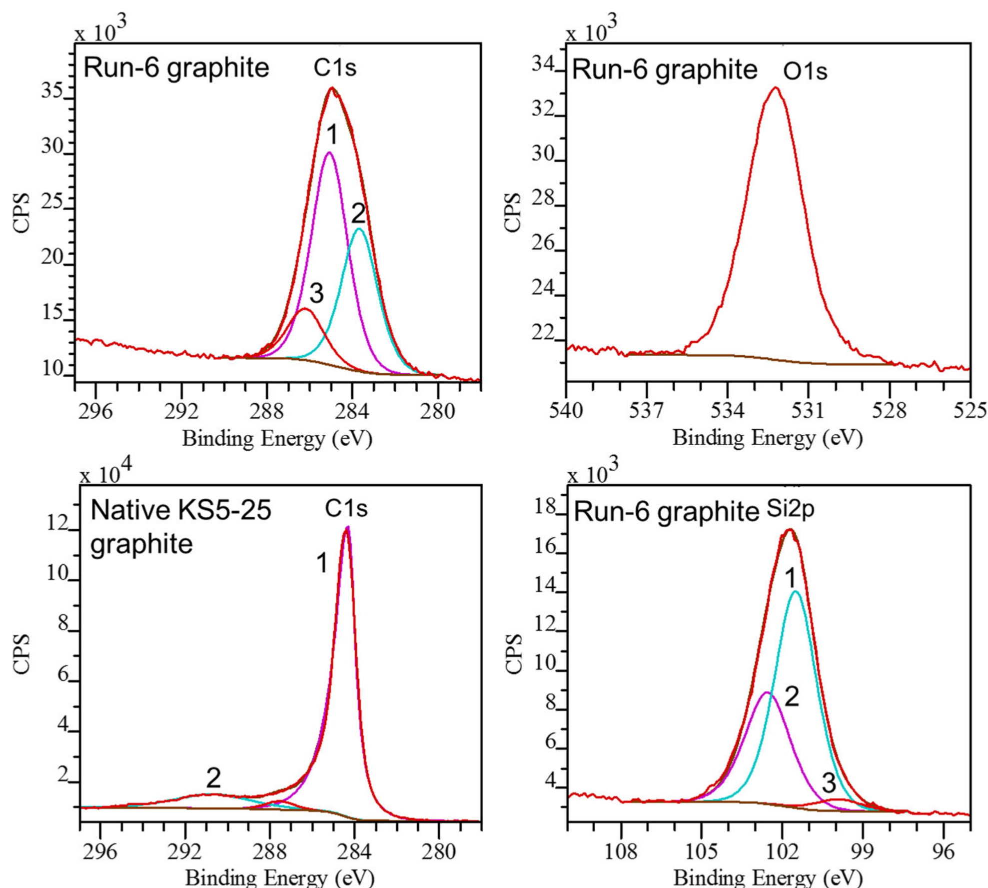

Fig. 4 XPS high-resolution spectra of native and plasma-coated graphite (run 6) micropowder with peak-fitting components

the Raman spectra (Fig. 3), whereas the O/C and O/Si ratios are respectively ca. 0.12 and 0.16, corresponding to a-$Si_{0.417}O_{0.062}C_{0.521}$:H, which emphasizes the scarce amount of oxygen as a simple process contaminant .

From the preliminary observation of the C1s high-resolution spectra in Fig. 4, it is evident that the C1s signal of the coated graphite shows a more symmetrical and broader-FWHM peak compared to the homologous signal of the native graphite (the FWHM values are reported in Table 2). Indeed, the C1s signal of pure graphite (maximum at 284.3 eV) has a narrow FWHM but is markedly asymmetrical due to the presence of a $\pi \rightarrow \pi^*$ shake-up transition in the higher-BE range (at 290.4 eV) [29]. By contrast, the C1s signal of plasma-coated graphite (maximum shifted to 285.0 eV) has a broader FWHM, because of various peak components arising from various chemical environments of carbon in the coating, but it features no asymmetrical tail in the higher-BE range [28].

Table 2 Surface elemental composition (atomic-percentage ratios) of plasma-coated graphite (run 6) micropowder

	Si / C [−]	O / C [−]	O / Si [−]
Plasma coating (run-6 graphite)	0.80 ± 0.01	0.12 ± 0.00	0.16 ± 0.00

Thus, the coating carbon is clearly distinguishable from the substrate carbon [30].

From the preliminary observation of the coating Si2p high-resolution signal (maximum at 101.7 eV), which is chemically shifted and broader in FWHM compared to the signal of pure silicon reported in literature (centered at 99 eV with a FWHM of 1.4 eV), it can be deduced that the monomer Si-Si bond is generally not retained in the coating and a fraction of the silicon atoms is oxidized [28]. As a consequence, the BE maximum of the coating O1s signal is expected to be in the range 532 to 533 eV, corresponding to the O-C bond and the O-Si bond, which is actually confirmed by the O1s high-resolution spectrum [28, 49].

Based on the above considerations, we then propose a peak-fitting model of C1s and Si2p high-resolution signals, shown in Fig. 4, with peak-fitting parameters and results reported in Table 3.

The native-graphite C1s signal was fitted with a sp^2-carbon component centered at 284.3 eV (1) plus a shake-up component at 290.4 eV (2) [29]. In contrast, the coated-graphite C1s signal was fitted with 3 components: a main sp^3-carbon component at 285.1 eV (1), taking into account both the adventitious-carbon layer above and a possible aliphatic-carbon environment in the coating, an intermediate component at 283.7 eV (2), which is attributed to the silicon-

Table 3 Peak-fitting parameters and results of the fitted high-resolution spectra in Fig. 4

Signal	Peak max. [eV]	Band and assignment	BE [eV]	FWHM [eV]	Line shape	Contr. [%]
C1s (native graphite)	284.4	1 sp^2 C–C	284.3	1.1	GL(90)T(0.9)	92.4
		2 Shake-up	290.4	4.1	GL(50)	6.0
		3 C=O	288.1	2.0	GL(50)	0.8
O1s (not shown)	533.5	1 O=C	533.5	–	no fitting, tiny signal	0.8
C1s (coated graphite)	285.0	1 sp^3 C–C	285.1	2.0	GL(50)	26.7
		2 CH_2–Si	283.7	2.0	GL(50)	17.9
		3 C–O	286.2	2.0	GL(50)	6.5
O1s	532.2	1 O–C / –Si	532.2	2.4	no fitting	6.5
Si2p	101.7	1 Si–CH_2	101.5	1.8	GL(50)	26.1
		2 Siloxanes	102.5	2.0	GL(50)	14.7
		3 Si–Si	99.9	2.0	GL(50)	1.6

bonded aliphatic (hydrogenated) carbon, and a side component at 286.2 eV (3), corresponding to the oxygen-bonded carbon of ether environment [28, 30–32, 46]. The Si2p signal was fitted with 3 components as well: a main component at 101.5 eV (1), attributable to the Si-CH_2 bonds, an intermediate component at 102.5 eV (2), attributable to the oxygen-bonded silicon of siloxane environment, and a small-area component at 99.9 eV (3), attributable to the scarce Si-Si bonds [28, 32, 33]. In fact, the Si-Si bond is the lowest-energy bond in the organosilicon molecules, the scission whereof is considered to be the initial step of the fragmentation mechanism of such molecules in a glow discharge, resulting in a coating which essentially consists of cross-linked -CH_2-Si-CH_2- segments [50, 51]. The oxygen is then likely to be embedded in the coating by bonding with couples of silicon atoms and also with couples of carbon atoms, so that the coating features minor XPS-detected siloxane and ether phases. Such a collateral process takes place during both the deposition process, when the reactor residual oxygen is likely to favor the breaking of the monomer Si-Si bond and the hydrogen detachment from the methyl groups, and the coating air exposure, when the coating free radicals tend to take up oxygen atoms to eliminate their dangling bonds [1, 46].

4 Conclusion

We performed a repeated PECVD reprocessing of fine graphite micropowder of 15 μm in average diameter with a downstream tubular reactor, in order to obtain a powder that is continuously covered by an organosilicon-plasma coating. FIB-SEM and powder-flowability assessments revealed that the coating initially consisted of a nanoparticle distribution, which progressively grew until a rough continuous coating was obtained after 6 process runs. The chemical characterization with Raman spectroscopy and X-ray photoelectron spectroscopy permitted to identify the main phase of the coating as amorphous hydrogenated silicon carbide, with minor siloxane and ether phases arising from the oxygen embedding in the coating during either the plasma deposition or the subsequent coating air exposure. The obtained result proves that the downstream-reactor PECVD is a valid technology to apply silicon-containing coatings onto particles of graphite micropowders.

Acknowledgements The Scientific Center for Optical and Electron Microscopy of the ETH Zürich is gratefully acknowledged for providing access to FIB-SEM facility and training. Prof. Dr. Antonella Rossi and Mr. Giovanni Cossu of the Department of Materials of the ETH Zürich are also gratefully acknowledged for providing access to XPS facility, training and technical support, while Dr. Robert Büchel of the Institute of Process Engineering of the ETH Zürich is gratefully acknowledged for providing training on Raman spectroscopy. Financial support comes from the Commission of Technology and Innovation and the Claude & Giuliana Foundation (Switzerland).

Publisher's Note Springer Nature remains neutral with regard to jurisdictional claims in published maps and institutional affiliations.

References

1. H. Yasuda, *Plasma Polymerization*, academic press Inc., USA 1985
2. Chapman B (1980) Glow Discharge Processes*: Sputtering and Plasma Etching*. Wiley, USA
3. V.R. Giampietro, Ph.D. Thesis, ETH Zurich, 2018
4. Jafari R, Tatoulian M (2011) F. Arefi-Khonsari. Reactive & Functional Polymers 71:520
5. Sonnenfeld A, Spillmann A, Arpagaus C, Rudolf von Rohr P (2009). Plasma Processes and Polymer 6:170
6. Inagaki N, Tasaka S, Ishij K (1993). J Appl Polym Sci 48:1433
7. Giampietro VR, Roth C, Gulas M, Wood V, Rudolf von Rohr P (2016). Plasma Process Polym 13:334
8. Xu C, Zhu J (2005). Chemical Engineering Science 60:6529

9. Bretagnol F, Tatoulian M, Arefi-Khonsari F, Lorang G, Amouroux J (2004). Reactive & Functional Polymers 61:221
11. Caquineau L, Aiche H, Vergnes B, Despax B (2012). Caussat, Surface & Coatings Technology 206:4814
12. Godfrey SP, Kinmond EJ, Badyal JPS, Little IR (2001). Chem Mater 13:513
13. Bayer C, Karches M, Matthews A, von Rohr PR (1998). Chemical Engineering & Technology 21:427
14. von Rohr PR, Borer B (2007). Chem Vap Depos 13:499
15. Borer B (2005) Ph. Rudolf von Rohr. Surface & Coatings Technology 200:377
16. Borer B, Sonnenfeld A (2006) Ph. Rudolf von Rohr. Surface & Coatings Technology 201:1757
17. Wei F, Zhu JX (1996). Journal of Chemical Engineering 64:345
18. Arpagaus C, Sonnenfeld A, Rudolf von Rohr P (2005). Chemical Engineering Technology 28:87
19. Roth C, Keller L, Rudolf von Rohr P (2012). Surface & Coating Technology 206:3832
20. B. Borer, Ph.D. Thesis, ETH Zurich, 2005
21. Roth C, Kuensch Z, Sonnenfeld A, Rudolf von Rohr P (2011). Surface & Coating Technology 205:S597
22. C. Roth, Ph.D. Thesis, ETH Zurich, 2012
23. Chung DDL (2002). Journal of Materials Science 37:1475
24. Terranova ML, Orlanducci S, Tamburri E, Guglielmotti V, Rossi M (2014). J Power Sources 246:167
25. Ferrari AC, Robertson J (2000). Phys Rev B 61:14095
26. Nisol B, Reniers F (2015). J Electron Spectrosc Relat Phenom 200: 311
27. Seah MP (2001). Surface Interface Analysis 31:721
28. G.E. Muilenberg (Ed.), *Handbook of X-ray Photoelectron* Spectroscopy, Perkin-Elmer Corporation (Physical Electronics Division), Eden Prairie, MN, 1979
29. Atzei D, Fantauzzi M, Rossi A, Fermo P, Piazzalunga A, Valli G, Vecchi R (2014). Appl Surf Sci 307:120
30. Alexander MR, Short RD, Jones FR (1996). J Mater Sci 31:1879
31. Nemanick EJ, Hurley PT, Webb LJ, Knapp DW, Michalak DJ, Brunschwig BS, Lewis NS (2006). J Phys Chem B 110:14770S
32. Beamson G, Briggs D (1992) *High Resolution XPS of Organic* Polymers*: The Scienta ESCA300* Database. Wiley, Chichester
33. Avila A, Montero I, Galán L, Ripalda JM, Levy R (2001). J Appl Phys 89:212
34. Scofield JH (1976). J Electron Spectrosc Relat Phenom 8:129
35. Reilman RF, Msezane A, Manson ST (1976). J Electron Spectrosc Relat Phenom 8:389
36. Seah MP, Dench WA (1979). Surf Interface Anal 1:2
37. Mayer C.K.K., Ph.D. Thesis, ETH Zurich, 2011
38. S. Hofmann, *Auger- and X-Ray Photoelectron* Spectroscopy *in* Materials Science, Springer-Verlag, Heidelberg, D, 2013
39. D. Schulze, Flow Properties of Powders and Bulk Solids, www.dietmar-schulze.com/grdle1.pdf (accessed February, 2014)
40. Robertson J (2002). Material Science and Engineering R37:129
41. Ding YS, Li WN, Iaconetti S, Shen XF, DiCarlo J, Galasso FS, Suib SL (2006). Surface & Coatings Technology 200:3041
42. Cançadoa LG, Takaia K, Enokia T, Endob M, Kimb YA, Mizusakib H, Spezialic NL, Jorioc A, Pimentac MA (2008). Carbon 46:272
43. Wang H, Yoshio M, Abe T, Ogumi Z (2002). J Electrochem Soc 149(4):A499
44. Choi WK, Loo FL, Ling CH, Loh FC, Tan KL (1995). J Appl Phys 78:7289
45. Choi WK, Chan YM, Ling CH, Lee Y, Gopalakrishnan R, Tan KL (1995). J Appl Phys 77:827
46. Nalwa HS (ed) (2001) *Silicon-Based Materials and Devices*. academic press, USA
47. Derst CWG, Bhatia KL, Kratschmer W, Kalbitzer S (1989). Appl Phys Lett 54:1722
48. Xu Z, He Z, Song Y, Fu X, Rommel M, Luo X, Hartmaier A, Zhang J, Fang F (2018). Micromachines 9(7):361
49. Annett Thøgersen JH, Selj ES (2012). Marstein, Journal of the Electrochemical Society 159(5):D276
50. Fonseca JLC, Badyal JPS (1992). Macromolecules 25:4730
51. Fonseca JLC, Tasker S, Apperley DC, Badyal JPS (1996). Macromolecules 29:17